

Crystallographic orientation and induced potential effects in photoelectron emission from metal surfaces by ultrashort laser pulses

C. A. Ríos Rubiano and R. Della Picca

CONICET and Centro Atómico Bariloche (CNEA) Bariloche, Argentina.

D. M. Mitnik

*Instituto de Astronomía y Física del Espacio (IAFE, CONICET-UBA),
Casilla de correo 67, sucursal 28, C1428EGA Buenos Aires, Argentina. and
Fac. de Ciencias Exactas y Naturales, Universidad de Buenos Aires.*

V. M. Silkin

*Donostia International Physics Center (DIPC), 20018 San Sebastián,
Spain, and Depto. de Física de Materiales, Facultad de Ciencias Químicas,
Universidad del País Vasco, Apdo. 1072, 20080 San Sebastián, Spain and
IKERBASQUE, Basque Foundation for Science, 48011 Bilbao, Spain*

M. S. Gravielle

*Instituto de Astronomía y Física del Espacio (IAFE, CONICET-UBA),
Casilla de correo 67, sucursal 28, C1428EGA Buenos Aires, Argentina.*

The influence of the crystallographic orientation of a typical metal surface, like aluminum, on electron emission spectra produced by grazing incidence of ultrashort laser pulses is investigated by using the band-structure-based-Volkov (BSB-V) approximation. The present version of the BSB-V approach includes not only a realistic description of the surface interaction, accounting for band structure effects, but also effects due to the induced potential that originates from the collective response of valence-band electrons to the external electromagnetic field. The model is applied to evaluate differential electron emission probabilities from the valence band of Al(100) and Al(111). For both crystallographic orientations, the contribution of partially occupied surface electronic states and the influence of the induced potential are separately analyzed as a function of the laser carrier frequency. We found that the induced potential strongly affects photoelectron emission distributions, opening a window to scrutinize band structure effects.

PACS numbers:

I. INTRODUCTION

In the last decade photoelectron emission (PE) from metal surfaces has received renewed attention as a result of the technological achievement of lasers with pulse durations of the order of attoseconds, which make it possible to study the behavior of electrons in condensed matter at their natural temporal orders [1–8]. Such a remarkable experimental progress needs to be accompanied by intensive theoretical research since the underlying quantum processes involve complex many-body mechanisms, whose complete understanding is still far from being achieved [9–16]. This paper aims to contribute to the study of PE from metal surfaces due to the interaction of ultrashort laser pulses with valence-band electrons. In particular, the article focuses on the influence of the crystallographic orientation of the surface on electron emission spectra, investigating the contributions of the surface-band structure and the induced surface potential for different crystal faces.

To describe the PE process we make use of a time-dependent distorted-wave method named band-structure-based-Volkov (BSB-V) approximation [17]. The BSB-V approach includes an accurate description

of the electron-surface interaction, given by the band-structure-based (BSB) model [18], while the action of the laser field on the emitted electron is represented by means of the Volkov phase [19]. The BSB model is based on the one-dimensional pseudopotential by Chulkov *et al.* [18, 20], which takes into account the electronic structure of the surface, replicating the width and position of the projected bulk energy gap and the surface and first image electronic states [21–25]. In this version of the BSB-V approximation we also incorporate the contribution of the induced surface potential, which is generated by the dynamic response of the metal surface to the laser field [26]. The induced potential is derived in a consistent way from the unperturbed BSB electronic states by using a linear response theory [27].

The BSB-V approximation, including the dynamic induced contribution, is applied to evaluate double-differential (energy- and angle- resolved) PE distributions for two different orientations of aluminum: Al(100) and Al(111). For both crystal faces, the influence of partially occupied surface electronic states (SEs) and the induced potential are examined by considering different parameters of the laser pulse. Our results indicate that the induced potential plays an important role in PE spec-

tra. It makes visible band structures signatures in PE spectra for the resonant case wherein the laser frequency coincides with the surface plasmon frequency, as well as for laser pulses with high carrier frequencies.

The article is organized as follows. In Sec. II we introduce the extended version of the BSB-V approximation, which takes into account the effect of the induced surface potential through a Volkov-type phase. In Sec. III results are shown and discussed, while our conclusions are summarized in Sec. IV. Atomic units are used unless otherwise stated.

II. THEORETICAL METHOD

Let us consider a finite laser pulse, characterized by a time-dependent electric field $\mathbf{F}_L(t)$, grazing impinging on a metal surface S . As a consequence of the interaction, a valence-band electron, initially in the state Φ_i , is ejected above the vacuum level, reaching a final state Φ_f . Within the framework of the time-dependent distorted wave formalism [28], the BSB-V transition amplitude for the electronic transition $\Phi_i \rightarrow \Phi_f$ reads [17]:

$$\mathcal{A}_{if} = -i \int_{-\infty}^{+\infty} dt \left\langle \chi_f^{(BSBV)}(\mathbf{r}, t) | \mathcal{V}(\mathbf{r}, t) | \Phi_i(\mathbf{r}, t) \right\rangle, \quad (1)$$

where

$$\mathcal{V}(\mathbf{r}, t) = \mathbf{r} \cdot \mathbf{F}_L(t) + V_I(\mathbf{r}, t) \quad (2)$$

is the perturbative potential at the time t and $\chi_f^{(BSBV)}(\mathbf{r}, t)$ is the final BSB-V distorted wave function, with \mathbf{r} the position vector of the active electron. The first term of Eq. (2) represents the interaction potential with the laser, expressed in the length gauge, while the second term, V_I , denotes the induced surface potential that is produced by electronic density fluctuations caused by the external field. The frame of reference is placed at the position of the crystal border, which is shifted outward with respect to the position of the topmost atomic layer by half of the interplanar distance, with the $\hat{\mathbf{z}}$ axis being oriented normal to the surface, pointing towards the vacuum region.

Within the BSB-V approach, the unperturbed states Φ_i and Φ_f are solutions of the Schrödinger equation associated with the one-dimensional electron-surface potential $V_S(z)$ given by Ref. [20], which depends on z , the component of \mathbf{r} perpendicular to the surface plane. Hence, the states $\Phi_i \equiv \Phi_{\mathbf{k}_{is}, n_i}(\mathbf{r}, t)$ and $\Phi_f \equiv \Phi_{\mathbf{k}_{fs}, n_f}(\mathbf{r}, t)$ can be expressed as

$$\Phi_{\mathbf{k}_s, n}(\mathbf{r}, t) = \frac{1}{2\pi} \exp(i\mathbf{k}_s \cdot \mathbf{r}_s) \phi_n(z) e^{-iEt}, \quad (3)$$

where \mathbf{k}_s (\mathbf{r}_s) is the component of the electron momentum (position vector) parallel to the surface plane, $\phi_n(z)$ is the one-dimensional eigenfunction with eigenenergy ε_n derived from the potential $V_S(z)$, and $E = k_s^2/2 + \varepsilon_n$ is the total electron energy.

According to the grazing incidence condition and the translational invariance of the problem in the plane parallel to the surface, the laser field is linearly polarized perpendicularly to the surface, that is, $\mathbf{F}_L(t) = F_L(t)\hat{\mathbf{z}}$, where the temporal profile of the pulse reads:

$$F_L(t) = F_0 \sin(\omega t + \varphi) \sin^2(\pi t/\tau), \quad (4)$$

for $0 < t < \tau$, and vanishes at all other times. In Eq. (4) F_0 represents the maximum field strength, ω is the carrier frequency, τ is the pulse duration, and φ is the carrier envelope phase, which is defined as $\varphi = (\pi - \omega\tau)/2$ for symmetric pulses. In this work we consider laser pulses with a fixed number N of full cycles inside the envelope; then, the pulse duration is defined as $\tau = NT$, with $T = 2\pi/\omega$ the laser oscillation period.

The induced potential V_I is evaluated from a linear response theory based on the BSB wave functions of Eq. (3) [29]. Making use of a slab geometry to derive the one-dimensional wave functions $\phi_n(z)$, the induced field $\mathbf{F}_I = -\nabla_{\mathbf{r}} V_I(\mathbf{r}, t)$ can be nearly expressed as

$$\mathbf{F}_I(z, t) = \begin{cases} F_I(t) \hat{\mathbf{z}} & \text{for } -d < z < 0, \\ 0 & \text{outside,} \end{cases} \quad (5)$$

where d is the width of the slab, formed by a sufficiently large number of atomic layers of the metallic crystal. The function

$$F_I(t) = -\frac{1}{2\pi} \int_{-\infty}^{\infty} d\nu \tilde{F}_L(\nu) f_I(\nu) e^{-i\nu t} \quad (6)$$

is the induced field inside the metal at the time t , with $\tilde{F}_L(\nu)$ denoting the Fourier transform of $F_L(t)$ and $f_I(\nu)$ being the dynamic response induced by a unitary and monochromatic electric field of frequency ν .

From Eqs. (2) and (5) it is possible to build $\chi_f^{(BSBV)}(\mathbf{r}, t)$ by introducing the distortions of both the external and the induced fields in the momentum distribution of the final state $\Phi_{\mathbf{k}_{fs}, n_f}$, by means of a Volkov-type phase [17, 26, 30]. It reads:

$$\chi_f^{(BSBV)}(\mathbf{r}, t) = \Phi_{\mathbf{k}_{fs}, n_f}(\mathbf{r} - \hat{\mathbf{z}} \alpha_L(t), t) \times \exp[iz A_{\text{tot}}(z, t) - i\beta_L(t)], \quad (7)$$

where the function

$$A_{\text{tot}}(z, t) = \begin{cases} A_L(t) + A_I(t) & \text{for } -d < z < 0, \\ A_L(t) & \text{outside,} \end{cases}$$

represents the position-dependent total vector potential at the time t , with

$$A_\mu(t) = - \int_{+\infty}^t dt' F_\mu(t'), \quad \mu = L, I, \quad (8)$$

being the vector potentials, with incoming asymptotic conditions, associated with the laser ($\mu = L$) and induced ($\mu = I$) fields, respectively. In turn, the functions

$$\alpha_L(t) = \int_{+\infty}^t dt' A_L(t'), \quad (9)$$

and

$$\beta_L(t) = \frac{1}{2} \int_{+\infty}^t dt' [A_L(t')]^2, \quad (10)$$

involved in Eq. (7), are respectively related to the quiver amplitude and the ponderomotive energy of the laser.

Finally, by replacing Eqs. (2), (3), and (7) in Eq. (1), the BSB-V transition amplitude, including the induced contribution, reduces to $\mathcal{A}_{if} = \delta(\mathbf{k}_{fs} - \mathbf{k}_{is}) a_{if}$, where the Dirac delta function imposes the momentum conservation in the plane parallel to the surface and

$$a_{if} = -i \int_0^{+\infty} dt R_{if}(t) e^{i[\Delta\varepsilon t + \beta_L(t)]} \quad (11)$$

represents the one-dimensional transition amplitude, with $\Delta\varepsilon = \varepsilon_{nf} - \varepsilon_{ni}$ being the energy gained by the electron during the process. The function R_{if} denotes the form factor given by

$$R_{if}(t) = \int_{-\infty}^{+\infty} dz \phi_{nf}^*(z - \alpha_L(t)) \phi_{ni}(z) g_f(z) \mathcal{V}(z, t) \times \exp[-i z A_{\text{tot}}(z, t)], \quad (12)$$

where $g_f(z) = e^{z\Theta(-z)/\lambda_f}$ accounts for the stopping of the ionized electron inside the material [17], with Θ being the unitary Heaviside function and $\lambda_f = \lambda(E_f)$ being the electron-mean-free path as a function of the final electron energy $E_f = k_{fs}^2/2 + \varepsilon_{nf}$.

Analogous to Ref. [17], the BSB-V differential probability of PE from the surface valence band can be expressed in terms of the one-dimensional transition amplitude of Eq. (11) as:

$$\frac{d^2 P}{dE_f d\Omega_f} = 2k_f \rho(k_{fz}) \sum_{n_i} |a_{if}|^2 \Theta(\tilde{k}_{n_i} - k_{fs}), \quad (13)$$

where Ω_f is the solid angle determined by the final electron momentum $\mathbf{k}_f = \mathbf{k}_{fs} + k_{fz}\hat{\mathbf{z}}$, with $k_{fz} = \sqrt{2\varepsilon_{nf}}$. The angle Ω_f is defined as $\Omega_f = (\theta_f, \varphi_f)$, where θ_f and φ_f are respectively the polar and azimuthal angles, with θ_f measured with respect to the surface plane. In Eq. (13), the sum indicates the addition over all the ϕ_{n_i} states with energies $\varepsilon_{n_i} \leq -E_W$ (E_W the function work), $\rho(k_{fz})$ is the density of final states ϕ_{n_f} with perpendicular momentum k_{fz} , and the factor 2 takes into account the spin states. The Heaviside function $\Theta(\tilde{k}_{n_i} - k_{fs})$ comes from the momentum conservation in the direction parallel to the surface plane, with $\tilde{k}_{n_i} = \sqrt{-2(\varepsilon_{n_i} + E_W)}$.

III. RESULTS

We apply the BSB-V approximation to simulate PE distributions from the valence band of Al(100) and Al(111). Since the ejection parallel to the polarization

vector of the laser field is expected to provide the major contribution to the PE rate [17], in this work we only consider electron emission normal to the surface plane, i.e., $\theta_f = 90$ deg. The maximum field strength was chosen as $F_0 = 10^{-3}$ a.u. (intensity $I_L = 3.52 \times 10^{-10}$ W/cm²), which belongs to the perturbative range, far from the damage threshold of the material [31].

The BSB-V differential probability was evaluated from Eq. (13) by varying the carrier frequency and the duration of the laser pulse. In the calculation, the BSB wave functions $\phi_n(z)$ were numerically derived by expanding them onto a basis of plane waves, defined as

$$\{\exp[i2\pi j(z + d/2)/D], j = -n_0, \dots, n_0\},$$

where $2n_0 + 1$ is the number of basis functions and D is the unit cell width, which acts as a normalization length. By using such an expansion in Eq. (12), the form factor $R_{if}(t)$ was reduced to a closed form in terms of the laser and induced fields, while the numerical integration on time involved in Eq. (11) was done with a relative error lower than 1%. Moreover, taking into account that the functions ϕ_{n_f} do not allow to distinguish electrons emitted inside the solid from those ejected towards the vacuum region, to evaluate the emission probability we averaged the contributions from the two different wave functions associated with the same positive energy ε_{nf} by considering that ionized electrons emitted to the vacuum region represent approximately a 50% of the total ionized electrons from the valence band [17, 32].

The parameters associated with the different orientations of aluminum are the followings. The Al(100) surface presents a work function $E_W = 0.161$ a.u. and an interplanar distance of 3.80 a.u., while the corresponding BSB wave functions $\phi_n(z)$ were obtained by using a basis of plane waves with $n_0 = 220$, a unit cell width $D = 342.04$ a.u., and a slab width $d = 266.00$ a.u. (i.e., 71 atomic layers). The Al(111) surface is characterized by a work function $E_W = 0.156$ a.u. and an interplanar distance of 4.39 a.u., and the $\phi_n(z)$ wave functions were evaluated using a plane wave basis with $n_0 = 170$, $D = 394.92$ a.u., and $d = 307.16$ a.u. (i.e., 71 atomic layers). Both faces of aluminum display the same Fermi energy, $E_F = 0.41$ a.u., and therefore, the same surface plasmon frequency $\omega_s = 0.40$ a.u., which characterizes the collective motion of valence-band electrons. The energy-dependent electron mean free-path $\lambda(E_f)$ was interpolated from data corresponding to the aluminum bulk, extracted from Ref. [33].

First, in order to provide an overall scenery of the influence of the aluminum crystal face, in Fig. 1 we compare PE distributions from Al(100) and Al(111) by considering a different number of cycles (rows) - $N = 2, 4$, and 6 - as well as different carrier frequencies (columns) - $\omega = 0.057, 0.4, 0.7$, and 1.5 a.u. For the lowest frequency (i.e., $\omega = 0.057$ a.u.), which corresponds to the experimental value for the Ti:sapphire laser system, PE spectra

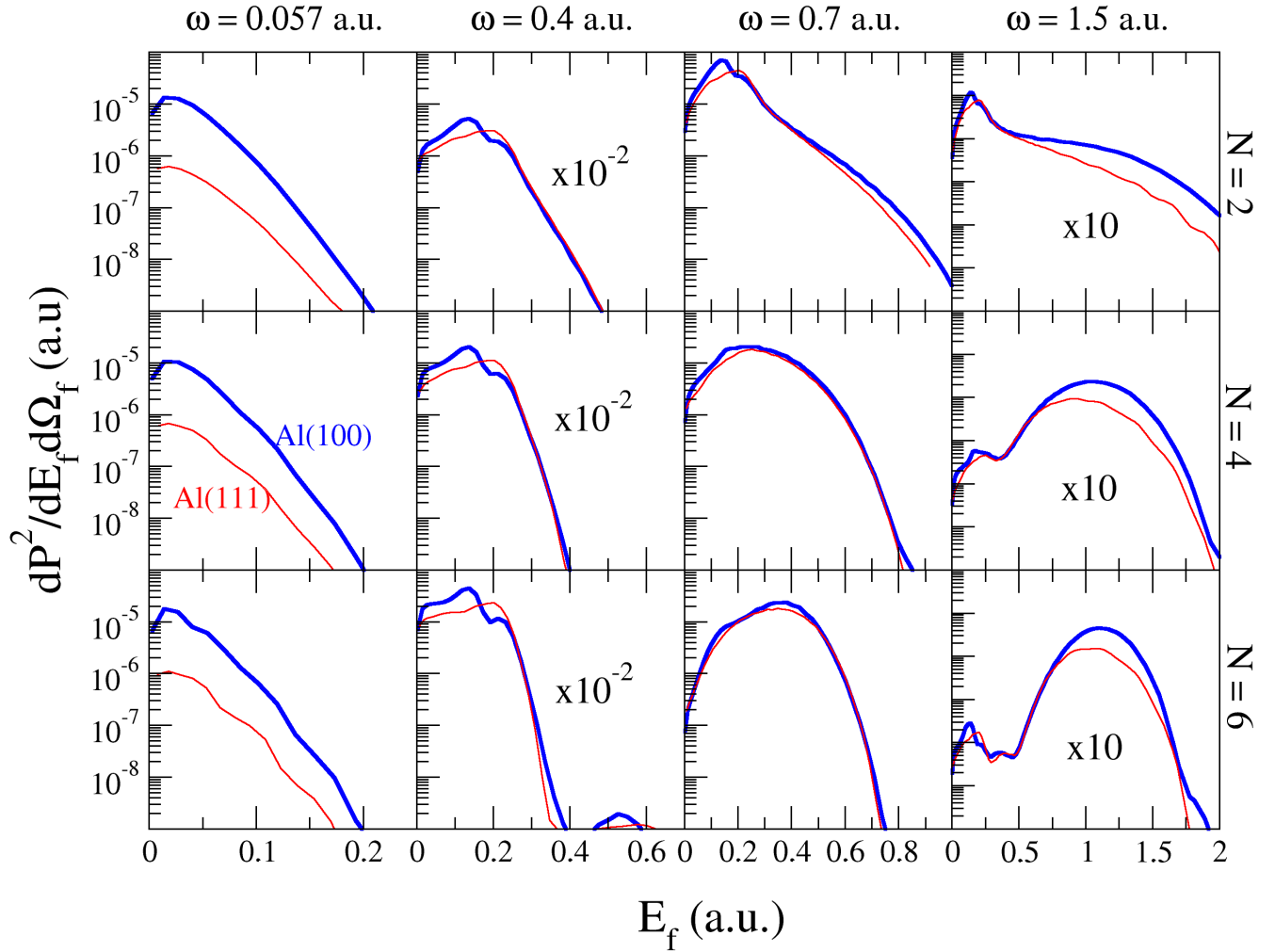


FIG. 1: (Color online) Double differential PE probabilities in the normal direction (i.e., $\theta_f = 90$ deg), as a function of the final electron energy E_f . Each column corresponds to a different carrier frequency of the laser pulse: $\omega = 0.057, 0.4, 0.7$ and 1.5 a.u. from left to right columns, respectively. Each row corresponds to a laser pulse with a different duration, that is, with $N = 2$ (upper row), $N = 4$ (middle row), and $N = 6$ (bottom row) cycles inside the envelope, respectively. In all panels, BSB-V results for two aluminium faces are displayed: Al(100), with blue thick lines, and Al(111), with red thin lines.

from the Al(100) surface are more than one order of magnitude higher than the ones corresponding to the Al(111) face. But when ω increases, emission probabilities from both aluminum faces become comparable in magnitude, departing appreciably each other only in the high energy region for high carrier frequencies, as observed for $\omega = 1.5$ a.u. Noticeably, for the intermediate frequency $\omega = 0.7$ a.u. the electron emission distributions from Al(100) and Al(111) are similar in the whole electron energy range. For this frequency, the small differences between the spectra corresponding to the different orientations for $N = 2$ disappear almost completely as N increases.

Concerning the influence of the pulse duration, it is more appreciable for high and intermediate frequencies. On the one hand, for short pulses, with only two cy-

cles inside the envelope, PE spectra (upper row of Fig. 1) present a maximal emission at low electron energies, with smoothly decreasing intensity as the velocity of ejected electrons augments. Noteworthy, for carrier frequencies in the range $\omega \gtrsim \omega_s$ this low-energy maximum presents a different structure depending on the crystal face. While for Al(111) it shows a single peak structure, for the Al(100) face the maximum displays double-hump features, which are particularly visible for the frequency $\omega = 0.4$ a.u. resonant with the surface plasmon frequency. In this particular case, the double structure is clearly observed even for long pulse durations, being related to the contribution of partially occupied SESs, as it will be discussed in Sec. III. A.

On the other hand, when the duration of the pulse increases to include several cycles inside the envelope, the

carrier frequency approximates to the photon energy and consequently, electron distributions become governed by the multiphoton mechanism associated with a Keldysh parameter $\gamma = \omega\sqrt{E_W}/F_0$ greater than the unity. For the higher frequencies - $\omega = 0.4, 0.7$ and 1.5 a.u. - the spectra of Fig. 1 corresponding to 4- and 6-cycle laser pulses display a broad maximum due to the absorption of one-photon of energy ω , which corresponds to the first of the above-threshold-ionization (ATI) peaks. This ATI maximum is roughly placed at $E_f \simeq \langle E_i \rangle - U_p + \omega$, where $\langle E_i \rangle$ is the initial energy averaged over all initial states, with $\langle E_i \rangle \simeq -0.44$ and -0.43 a.u. for Al(100) and Al(111) respectively, and $U_p = F_0^2/(4\omega^2)$ is the ponderomotive energy, which results negligible in the present cases. The width of these ATI peaks depends on the pulse duration, decreasing as τ increases [26], as also observed in PE from atoms [34]. However, in contrast to the atomic case, the electron emission from metal surfaces presents a lower limit in the width of the ATI peaks, which is produced by the energy spread of the metal valence band, characterized by the Fermi energy. This fact causes the absence of ATI structures in the multiphotonic spectra for $\omega = 0.057$ a.u. (left lower panels of Fig. 1) because the energy difference between consecutive ATI peaks is much lower than the width of each peak.

From Fig. 1 it is also observed that the multiphotonic spectra for $\omega = 1.5$ a.u. (right lower panels) show different structures in the low energy region, depending on the crystallographic orientation of the surface. The origin of such crystal face effects can be attributed to two different contributions: the emission from partially occupied SESs and the induced potential. These contributions will be separately analyzed in the following subsections.

A. Photoelectron emission from SESs

One of the most remarkable effects of the crystal band structure is the presence of partially occupied SESs, which display a highly localized electron density at the edge of the crystal surface, favoring the release of electrons from the material. Even though for high carrier frequencies, SESs were found to play a minor role in PE spectra from Al(111) [17], the relative importance of the SES contribution varies with the crystallographic orientation and the parameters of the laser pulse. In Fig. 2, we plot the surface potential $V_S(z)$ for Al(100) and Al(111), together with the square modulus of the corresponding SESs, $|\phi_{SES}(z)|^2$, with eigenenergies $\varepsilon_{SES} = -0.263$ a.u. and $\varepsilon_{SES} = -0.32$ a.u., respectively. The average depth of the potential well, defined as $V_{S0} = E_F + E_W$, is similar for both orientations. However, the corrugation of $V_S(z)$ for the (100) face is almost a factor 6 larger than the one corresponding to the (111) orientation, producing a stronger localization of the SESs of Al(100) close to the surface border, as observed in Fig. 2.

The marked difference between the SES densities of both aluminum faces at the crystal border can be traced

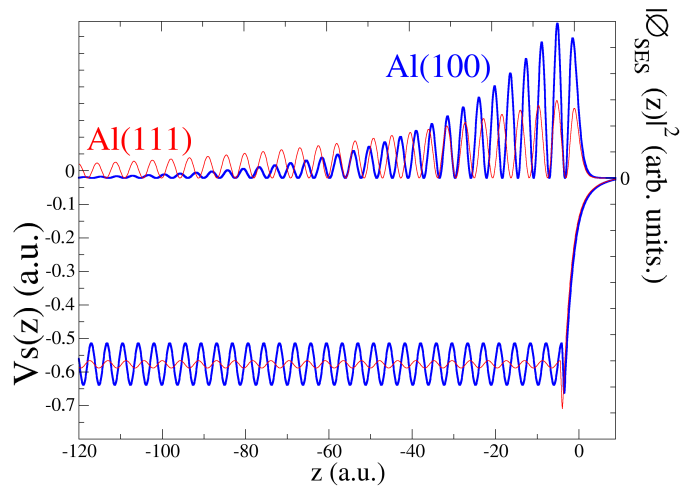


FIG. 2: (Color online) Potential $V_S(z)$ (lower graph), together with the square modulus of the corresponding SESs, $|\phi_{SES}(z)|^2$ (upper graph), for Al(100), with blue thick lines, and for Al(111), with red thin lines.

from the superimposed structures of the PE spectra corresponding to the resonant frequency $\omega \simeq \omega_s = 0.4$ a.u. For a 6-cycle laser pulse with $\omega = 0.4$ a.u., in Fig. 3 we compare differential emission probabilities from Al(100) and Al(111) with partial values due to emission from SESs as well as from states at the top of the valence band. Despite the general shape of the spectra of Fig. 3 is not affected by the crystallographic orientation, a closer examination of the first ATI peak reveals the presence of different superimposed structures for each face, as also observed in Fig. 1. For Al(100) the first ATI peak displays a double-bump structure, with two bulges peaking at $E_f \approx 0.14$ a.u. and $E_f \approx 0.24$ a.u. respectively, whereas for Al(111) only one maximum at $E_f \approx 0.24$ a.u. exists. This latter maximum, present for the two faces, is placed at $E_f \simeq -E_W + \omega$, corresponding to one-photon absorption from initial states at the top of the valence band, whose partial contribution is also displayed in the figure. Instead, the peak at $E_f \sim 0.14$ a.u., only visible in the Al(100) spectrum, is produced by the absorption of one-photon from partially occupied SESs, being placed at $E_f \simeq \varepsilon_{SES} + \omega$. From the comparison of Figs. 3 (a) and (b) we conclude that the presence or absence of SES signatures in the PE distribution, depending on the crystal face, is associated with the mayor or minor localization of the electronic density of SESs at the crystal border. For Al(100) such a localization is more than three times higher than the one corresponding to Al(111), making its contribution clearly discernible in the PE spectrum. While for Al(111), the SES contribution results completely concealed by emission from other initial states, which washes out SES footprints from the electron distribution. Therefore, PE spectra under resonant conditions might offer an attractive window to obtain information about the surface band structure. Besides, in the reso-

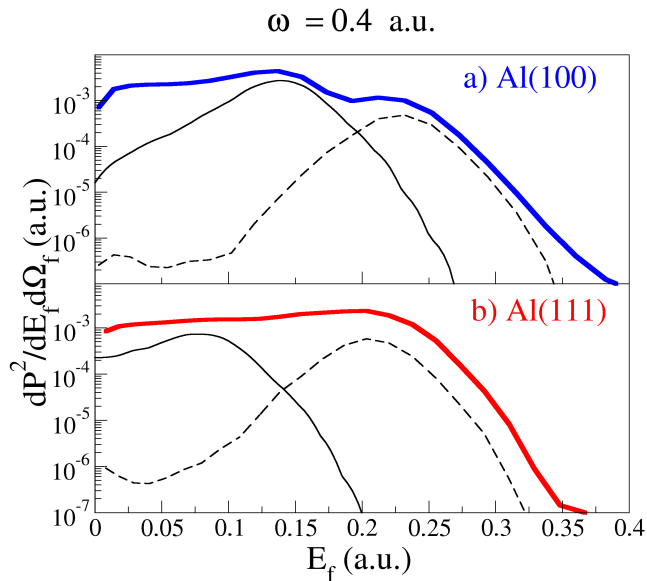


FIG. 3: (Color online) PE distribution in the normal direction, as a function of the final electron energy, for a 6-cycle laser pulse with a carrier frequency $\omega = 0.4$ a.u. BSB-V results for (a) Al(100) and (b) Al(111) are displayed in the upper and lower panels, respectively. In both panels, the thick solid line corresponds to the emission probability from the valence band, and the black thin dashed and solid lines, to partial contributions from the top of the valence band and partially occupied SESs, respectively.

nant case the contribution of the plasmon decay mechanism should be also included, producing an additional structure just at the electronic energy $E_f \simeq \omega_s$.

Previous band-structure effects disappear as the carrier frequency departs from the resonant one. But noteworthy they become again visible for high frequencies, as shown in Fig. 4. In this figure we consider electron emission from Al(100) and Al(111) for a laser pulse with $\omega = 1.5$ a.u. and 6 cycles. In this case, different low-energy structures are present in the PE spectra for the two faces. The low-energy hump due to ejection of slow electrons from the top of the valence band is again visible for both faces, while the one associated with emission from SESs is appreciable only for the (100) face. As discussed above, this is a consequence of the different corrugation and SES electronic density of the two crystallographic orientations. The observation of such effects significantly depends on the action of the induced potential. Furthermore, even though for high frequencies these low-energy structures are less noticeable than in the resonant case, they might still provide information about the relative importance of SES contributions.

B. Induced potential effects

With the aim of understanding how the collective response of valence-band electrons to the laser field affects

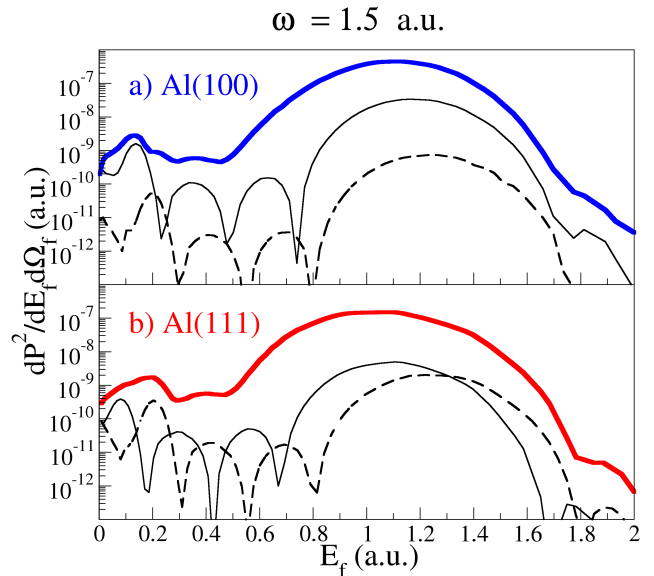


FIG. 4: (Color online) Analogous to Fig. 3 for $\omega = 1.5$ a.u.

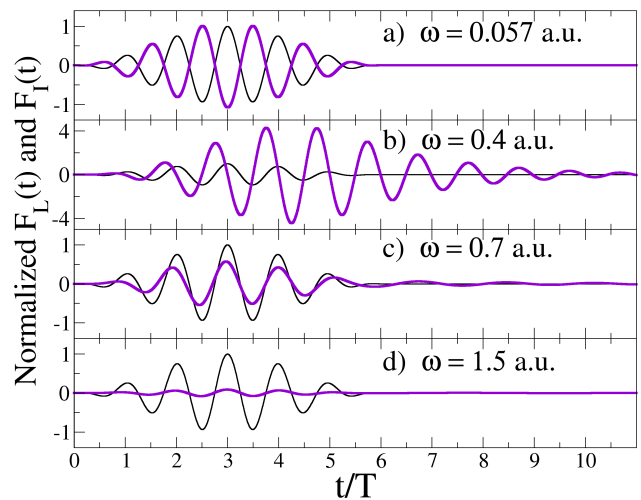


FIG. 5: (Color online) Normalized laser and induced fields, as a function of the normalized time t/T , for a 6-cycle laser pulse impinging on Al(111). The carrier frequency of the laser pulse is: a) $\omega = 0.057$ a.u., b) $\omega = 0.4$ a.u., c) $\omega = 0.7$ a.u., and d) $\omega = 1.5$ a.u. In all panels, black thin line, normalized laser field $F_L(t)/F_0$; violet thick line, normalized induced field $F_I(t)/F_0$.

the distribution of emitted electrons, in this subsection we examine the contribution of the induced field to PE spectra.

For laser pulses with several oscillations, the electronic rearrangement induced in the metal by the external perturbation strongly depends on the carrier frequency. To illustrate such a variation, in Fig. 5 we plot the laser and induced fields for 6-cycle laser pulses, with different frequencies, impinging on the Al(111) surface. For frequencies much lower than ω_s , like $\omega = 0.057$ a.u., the induced

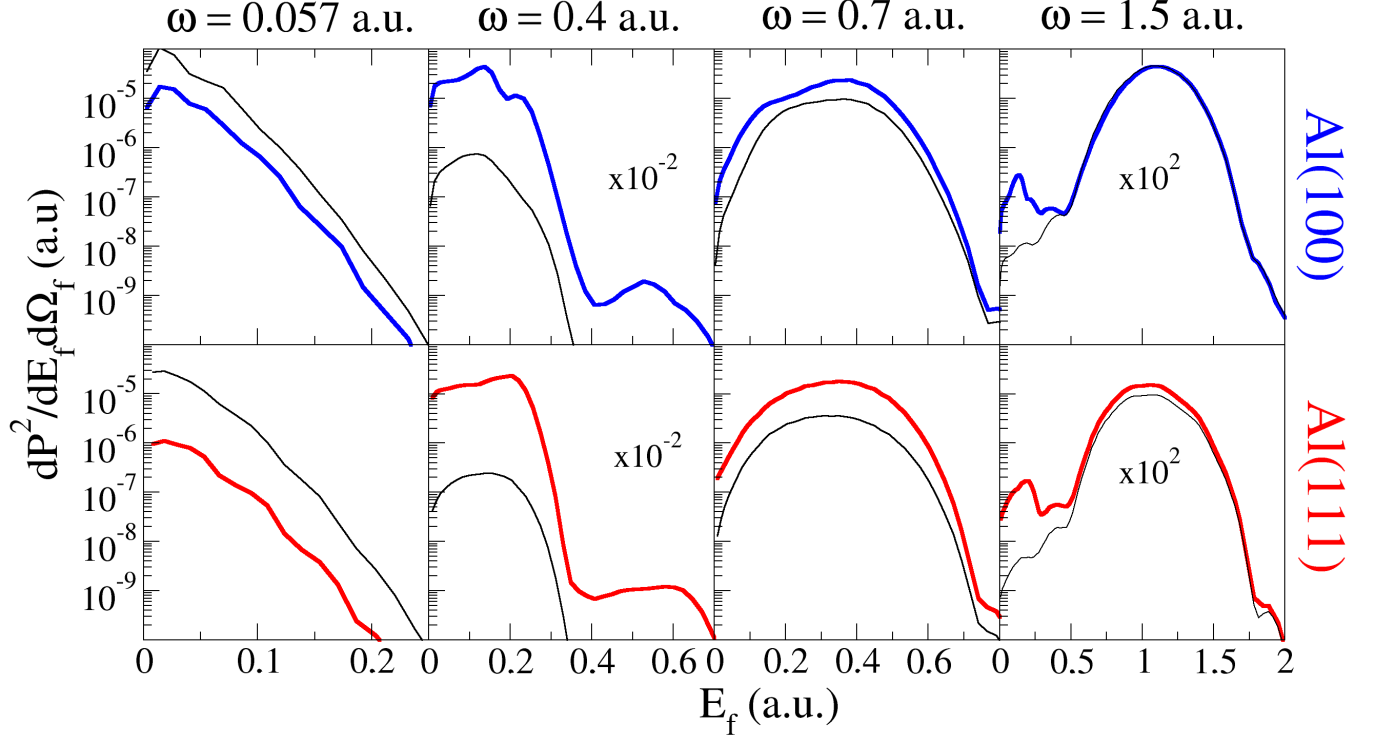


FIG. 6: (Color online) PE distribution from the valence band of both aluminum faces - Al(100) (upper row) and Al(111) (lower row) - as a function of the final electron energy. The impinging 6-cycle laser pulse has a carrier frequency $\omega = 0.057, 0.4, 0.7$ and 1.5 a.u. from left to right columns, respectively. Thick (thin) solid lines, BSB-V results obtained including (without including) the induced potential.

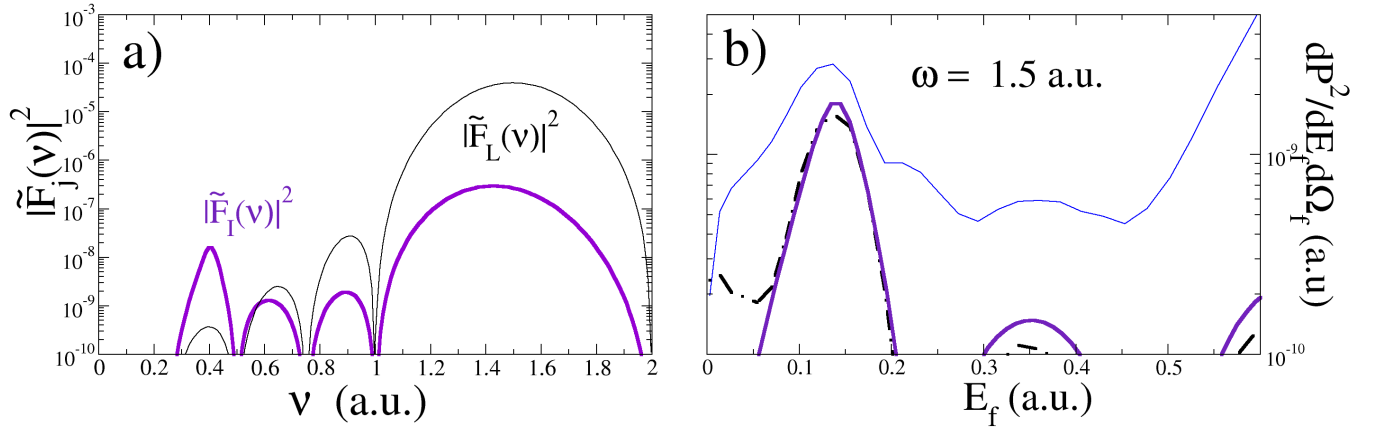


FIG. 7: (Color online) Analysis of the frequency domain distribution of partial contributions to PE from the valence band of Al(100) by a 6-cycle laser pulse with $\omega = 1.5$ a.u. (a) Frequency profiles of the laser and induced fields, as a function of the frequency. The Fourier transform of the laser field \tilde{F}_L (induced field \tilde{F}_I) is displayed with black thin (violet thick) solid line. (b) The BSB-V PE distribution, as a function of the electron energy, is shown with blue thin line, and the SES contribution with black dot-dashed line. The Fourier transform contribution, $|\tilde{F}_{tot}(E_f + \varepsilon_{SES})|^2$ (in arb. units), is plotted with violet solid line.

and external fields are similar in strength but in counterphase, tending to the static limit in which the total electric field vanishes inside the metal. But when the frequency augments to reach the resonant value $\omega \simeq \omega_s = 0.4$ a.u., the maximum strength of $F_I(t)$ is four times larger than F_0 ; therefore, the total field inside the metal becomes dominated by the induced response of the metal surface. In turn, for $\omega > \omega_s$ surface electrons try to follow the external field, in such a way that the laser and induced fields oscillate almost with the same phase, but the intensity of the induced field decreases steeply as the carrier frequency augments.

The meaningful differences among the induced responses for different frequencies of the external field, observed in Fig. 5, are directly reflected in their contributions to the electron emission process. In Fig. 6 we compare BSB-V differential emission probabilities, derived from Eq. (13), with BSB-V values obtained without including the induced surface interaction, that is, by fixing $F_I(t) = A_I(t) = 0$, considering the same laser parameters as in Fig. 5. Results for both crystallographic orientations -Al(100) (upper panels) and Al(111) (lower panels)- are displayed in the figure. From Fig. 5 (a), for $\omega = 0.057$ a.u. the induced response screens the laser field inside the metal almost completely. Then, in this case the inclusion of the induced potential causes a marked reduction of the PE yield, this effect being stronger for Al(111) than for Al(100). Instead, for $\omega = 0.4$ a.u. the laser pulse becomes resonant with ω_s , originating a large increase of the emission probability, greater than two order of magnitude. Notice that for this resonant frequency, the induced field is not only higher than the external field but also it persists twice the original pulse duration (see Fig. 5 (b)), contributing to augment the emission probability after the external field turned off. For a carrier frequency slightly higher than the surface plasmon frequency, like $\omega = 0.7$ a.u., the induced field goes on reinforcing the action of the laser pulse, although its intensity is four times lower than that corresponding to the resonant case, as shown in Fig. 5 (c). Hence, the inclusion of induced potential within the BSB-V approach produces a moderate increase of the PE probability, being again higher for the (111) face.

The case of $\omega = 1.5$ a.u., shown in the right column of Fig. 6, deserves further discussion. For such a high frequency, electrons are not able to follow the quick variation of the external perturbation and consequently, the maximum strength of $F_I(t)$ is more than one order of magnitude lower than the one of the laser field, as displayed in Fig. 5 (d). As it was expected, this small induced response does not affect appreciably the main electron emission, which occurs around the first ATI peak. However, we remarkably found that the induced potential introduces a pronounced growth of the probability at low electron energies, just in the region where the double-hump low-energy structure associated with SES emission

appears in the Al(100) case. To investigate in detail this unforeseen contribution, in Fig. 7 (a) we plot the decomposition in frequencies of both the laser ($\tilde{F}_L(\nu)$) and the induced field ($\tilde{F}_I(\nu)$) for this case. The utility of analyzing the frequency domain of the fields lies on the fact that the PE spectrum can be roughly estimated as proportional to the square modulus of the Fourier transform of the total electric field, that is, $|\tilde{F}_{tot}(\nu)|^2$, evaluated at $\nu = E_f + E_i$, with $\tilde{F}_{tot}(\nu) = \tilde{F}_L(\nu) + \tilde{F}_I(\nu)$ and E_i covering the energy range of all initially occupied states. In Fig. 7 (a), although the Fourier transform of the laser field is several orders of magnitude higher than the one of the induced field around the carrier frequency, $\tilde{F}_I(\nu)$ retains a peak associated with the resonance $\nu \cong \omega_s$, which largely overpasses the value of $\tilde{F}_L(\omega_s)$. This resonant peak is found to be the origin of the low-energy SES contribution of the spectrum for Al(100), as shown in Fig. 7 (b), where we observe that the curve corresponding to $|\tilde{F}_{tot}(E_f + \varepsilon_{SES})|^2$ (multiplied by an arbitrary factor) almost coincides with the SES contribution.

IV. CONCLUSIONS

We have studied PE spectra produced by the interaction of ultrashort laser pulses with the valence band of two different faces of aluminium - Al(100) - Al(111) - by using of the BSB-V approximation. In the present version of the BSB-V approach we have incorporated the contribution of the induced field, originated from the collective response of surface electrons to the external perturbation. We found that the induced response of the metal surface strongly affects electron emission distributions for a wide range of laser frequencies, including high ω - values. In the resonant case with the surface plasmon frequency, the effect of the induced field contributes to make visible signatures coming from partially occupied SESs of the Al(100) surface, while for Al(111) these SES structures are completely washed out by emission from other initially occupied states. Similar features are also observed in the low-energy region of the spectra for high carrier frequencies of the laser pulse, for which the influence of the induced potential was expected negligible. These findings open the way to investigate band structure effects by varying the parameters of the laser pulse, the crystal orientation, and the observation region.

Acknowledgments

Financial support from CONICET, UBA, and AN-PCyT of Argentina is acknowledged.

-
- [1] A. L. Cavalieri, N. Muller, Th Uphues, V. S. Yakovlev, A. Baltuska, B. Horvath, B. Schmidt, L. Blumel, R. Holzwarth, S. Hendel, M. Drescher, U. Kleineberg, P. M. Echenique, R. Kienberger, F. Krausz, and U. Heinzmann. Attosecond spectroscopy in condensed matter. *Nature*, 449(7165):1029–1032, Oct 2007.
- [2] L. Miaja-Avila, C. Lei, M. Aeschlimann, J. L. Gland, M. M. Murnane, H. C. Kapteyn, and G. Saathoff. Laser-Assisted Photoelectric Effect from Surfaces. *Phys. Rev. Lett.*, 97:113604, Sep 2006.
- [3] L. Miaja-Avila, G. Saathoff, S. Mathias, J. Yin, C. Laovorakiat, M. Bauer, M. Aeschlimann, M. M. Murnane, and H. C. Kapteyn. Direct Measurement of Core-Level Relaxation Dynamics on a Surface-Adsorbate System. *Phys. Rev. Lett.*, 101:046101, Jul 2008.
- [4] G. Saathoff, L. Miaja-Avila, M. Aeschlimann, M. M. Murnane, and H. C. Kapteyn. Laser-assisted photoemission from surfaces. *Phys. Rev. A*, 77:022903, Feb 2008.
- [5] L. Miaja-Avila, J. Yin, S. Backus, G. Saathoff, M. Aeschlimann, M. M. Murnane, and H. C. Kapteyn. Ultrafast studies of electronic processes at surfaces using the laser-assisted photoelectric effect with long-wavelength dressing light. *Phys. Rev. A*, 79:030901, Mar 2009.
- [6] S. Mathias, M. Wiesenmayer, F. Deicke, A. Ruffing, L. Miaja-Avila, M. M. Murnane, H. C. Kapteyn, M. Bauer, and M. Aeschlimann. Time and angle resolved photoemission spectroscopy using femtosecond visible and high-harmonic light. *Journal of Physics: Conference Series*, 148(1):012042, 2009.
- [7] S. Neppel, R. Ernstorfer, E. M. Bothschafter, A. L. Cavalieri, D. Menzel, J. V. Barth, F. Krausz, R. Kienberger, and P. Feulner. Attosecond Time-Resolved Photoemission from Core and Valence States of Magnesium. *Phys. Rev. Lett.*, 109:087401, Aug 2012.
- [8] S. Neppel, R. Ernstorfer, A. L. Cavalieri, C. Lemell, G. Wachter, E. Magerl, E. M. Bothschafter, M. Jobst, M. Hofstetter, U. Kleineberg, J. V. Barth, D. Menzel, J. Burgdorfer, P. Feulner, F. Krausz, and R. Kienberger. Direct observation of electron propagation and dielectric screening on the atomic length scale. *Nature*, 517(7534):342–346, Jan 2015. Letter.
- [9] M. N. Faraggi, M. S. Gravielle, and D. M. Mitnik. Interaction of ultrashort laser pulses with metal surfaces: Impulsive jellium-Volkov approximation versus the solution of the time-dependent Schrödinger equation. *Phys. Rev. A*, 76:012903, Jul 2007.
- [10] E. E. Krasovskii. Attosecond spectroscopy of solids: Streaking phase shift due to lattice scattering. *Phys. Rev. B*, 84:195106, Nov 2011.
- [11] C. Lemell, S. Neppel, G. Wachter, K. Tókési, R. Ernstorfer, P. Feulner, R. Kienberger, and J. Burgdorfer. Real-time observation of collective excitations in photoemission. *Phys. Rev. B*, 91:241101, Jun 2015.
- [12] A. G. Borisov, D. Sánchez-Portal, A. K. Kazansky, and P. M. Echenique. Resonant and nonresonant processes in attosecond streaking from metals. *Phys. Rev. B*, 87:121110, Mar 2013.
- [13] Q. Liao and U. Thumm. Attosecond Time-Resolved Photoelectron Dispersion and Photoemission Time Delays. *Phys. Rev. Lett.*, 112:023602, Jan 2014.
- [14] Renate Pazourek, Stefan Nagele, and Joachim Burgdorfer. Attosecond chronoscopy of photoemission. *Rev. Mod. Phys.*, 87:765–802, Aug 2015.
- [15] J. C. Baggese and L. B. Madsen. Theory for time-resolved measurements of laser-induced electron emission from metal surfaces. *Phys. Rev. A*, 78:032903, Sep 2008.
- [16] H. Jouin, M. Raynaud, G. Duchateau, G. Geoffroy, A. Sadou, and P. Martin. Quantum-classical model for the surface plasmon enhanced photoemission process at metal surfaces. *Phys. Rev. B*, 89:195136, May 2014.
- [17] C. A. Rios Rubiano, M. S. Gravielle, D. M. Mitnik, and V. M. Silkin. Band-structure effects in photoelectron-emission spectra from metal surfaces. *Phys. Rev. A*, 85:043422, Apr 2012.
- [18] E.V. Chulkov, V.M. Silkin, and P.M. Echenique. Image potential states on metal surfaces: binding energies and wave functions. *Surface Science*, 437(3):330 – 352, 1999.
- [19] D.M. Wolkow. über eine klasse von lsungen der diracschen gleichung. *Zeitschrift fr Physik*, 94(3-4):250–260, 1935.
- [20] E.V. Chulkov, V.M. Silkin, and P.M. Echenique. Image potential states on lithium, copper and silver surfaces. *Surface Science*, 391(1):L1217 – L1223, 1997.
- [21] P M Echenique and J B Pendry. The existence and detection of Rydberg states at surfaces. *Journal of Physics C: Solid State Physics*, 11(10):2065, 1978.
- [22] F Finocchi, C.M. Bertoni, and S Ossicini. Surface Science Section Simple metal surfaces and image potential states. *Vacuum*, 41(1):535 – 537, 1990.
- [23] Leszek Jurczyk and Maria Stlicka. Barrier-resonance states in an external electric field. *Surface Science*, 266(1):141 – 144, 1992.
- [24] M. Nekovee and J. E. Inglesfield. Threshold Behaviour of Surface Density of States at the Vacuum Level. *EPL (Europhysics Letters)*, 19(6):535, 1992.
- [25] P.M. Echenique, R. Berndt, E.V. Chulkov, Th. Fauster, A. Goldmann, and U. Hfer. Decay of electronic excitations at metal surfaces. *Surface Science Reports*, 52(78):219 – 317, 2004.
- [26] Marisa Faraggi, Iñigo Aldazabal, Maria Silvia Gravielle, Andres Arnau, and Vyacheslav M. Silkin. Study of the induced potential produced by ultrashort pulses on metal surfaces. *J. Opt. Soc. Am. B*, 26(12):2331–2336, Dec 2009.
- [27] M. Alducin, V. M. Silkin, J. I. Juaristi, and E. V. Chulkov. Energy loss of ions at metal surfaces: Band-structure effects. *Phys. Rev. A*, 67:032903, Mar 2003.
- [28] D.P. Dewangan and J. Eichler. Charge exchange in energetic ion-atom collisions. *Physics Reports*, 247(24):59 – 219, 1994.
- [29] V M Silkin, A K Kazansky, E V Chulkov, and P M Echenique. Time-dependent screening of a point charge at a metal surface. *Journal of Physics: Condensed Matter*, 22(30):304013, 2010.
- [30] P. A. Macri, J. E. Miraglia, and M. S. Gravielle. Ionization of hydrogen targets by short laser pulses. *J. Opt. Soc. Am. B*, 20(9):1801–1806, Sep 2003.
- [31] C. Lemell, X.-M. Tong, F. Krausz, and J. Burgdorfer. Electron Emission from Metal Surfaces by Ultrashort Pulses: Determination of the Carrier-Envelope Phase. *Phys. Rev. Lett.*, 90:076403, Feb 2003.

- [32] M. N. Faraggi, M. S. Gravielle, and V. M. Silkin. Quantum-mechanical model for valence-electron emission from metal surfaces. *Phys. Rev. A*, 69:042901, Apr 2004.
- [33] David R. Penn. Electron mean-free-path calculations using a model dielectric function. *Phys. Rev. B*, 35:482–486, Jan 1987.
- [34] V. D. Rodriguez, E. Cormier, and R. Gayet. Ionization by short uv laser pulses: Secondary above-threshold-ionization peaks of the electron spectrum investigated through a modified Coulomb-Volkov approach. *Phys. Rev. A*, 69:053402, May 2004.